The 2020 Eruption and Large Lateral Dike Emplacement at Taal Volcano, Philippines: Insights from Satellite Radar Data

Bato et al., 2021

Summary

- Methods: Use C- and L-band InSAR – time series of unwrapped interferograms; modelled deformation - pre- (inflation), co- (deflation, dike emplacement), and post-eruption (dike propagation)
- Results: Pre – see long term trend of decreasing LOS displacement and then increase in months prior to eruption – infer a growing reservoir at ~5 km depth; Co – volume loss >> short-term growth, infer large dike intrusion (> volume loss from reservoir), Post – minor opening, inflation
- Discussion – long term depressurizing and degassing → sudden magma injection, dike propagation in favorable orientation (fault zone), interaction w/ hydrothermal system (gas loss) – not an eruption

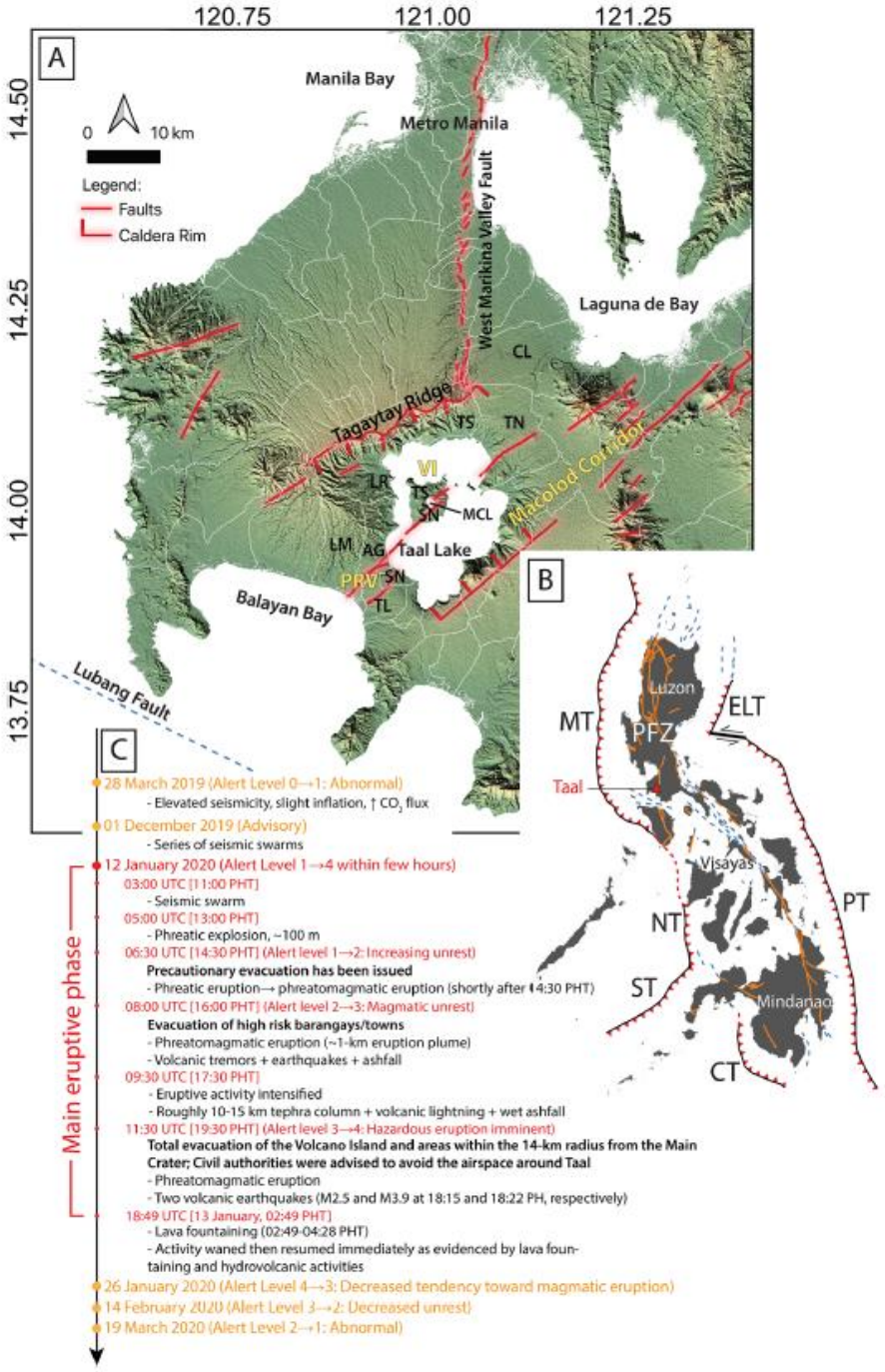

(a) Map showing Taal volcano and the local tectonic features in the vicinity including parts of the Macolod Corridor (modified after Delos Reyes et al., 2018; Pubellier et al., 2000; Rimando & Knuepfer, 2006). VI: Volcano Island; PRV: Pansipit River Valley; MCL: Main Crater Lake. White outlines are town boundaries. LM: Lemery; AG: Agoncillo; LR: Laurel; TL: Taal; SN: San Nicolas; TS: Talisay; CL: Calamba; TN: Tanauan. (b) The Philippine archipelago and the major tectonics controlling the region. Two opposing subduction zones create the oblique convergence in the Philippines: to the west are the Manila-Negros-Sulu and Cotabato trenches, and to the east is the Philippine Trench. The result of this oblique plate motion is the Philippine Fault Zone which is a 1,200-km long left-lateral strike-slip fault that traverses the archipelago from north to south (Aurelio, 2000). Orange solid lines are active faults and blue broken lines are offshore extension of the active faults. The red triangle is the location of Taal volcano. MT: Manila Trench, NT: Negros Trench, ST: Sulu Trench, ELT: East Luzon Trough, PFZ: Philippine Fault Zone, CT: Cotabato Trench, PT: Philippine Trench. (c) Summarized chronology of events based on issued PHIVOLCS bulletins and publicly available materials (Martinez-Villegas, 2020).

Fig 1

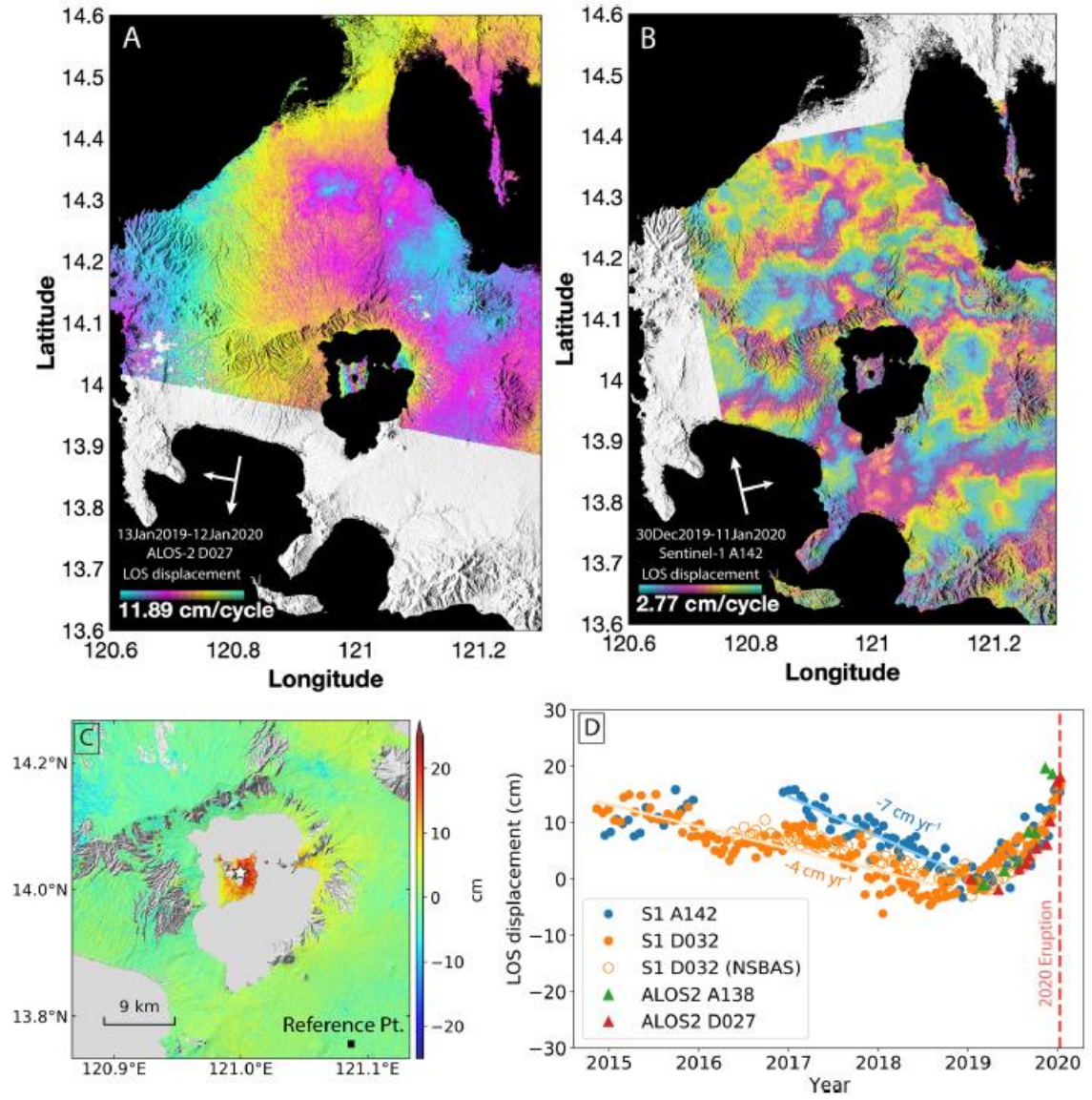

Figure 2. (a and b) Pre-eruptive interferograms of Taal produced using (a) ALOS-2 L-band and (b) Sentinel-1 C-band satellite data set showing long- and short-term surface deformations, respectively. (c) Cumulative descending LOS displacement map from Sentinel-1 track 032, covering January 2, 2019–January 9, 2020. (d) Surface LOS displacement time-series measured at 14.0188° N, 121.0012° E (i.e., star symbol in Figure 2c) from both the ascending and descending tracks of ALOS-2 and Sentinel-1 starting in late 2014 and leading up to the January 12, 2020 Taal eruption (dashed red line). For each time-series, we referenced the date to their respective first acquisitions in January 2019 (ALOS-2 A138: 22 January 2019; ALOS-2 D027: January 13, 2019; S1 A142: January 4, 2019; S1 D032: January 2, 2019) Blue dots: displacement time-series from Sentinel-1 ascending track 142. Orange dots: displacement time-series from Sentinel-1 descending track 032. Orange circles: displacement time-series from Sentinel-1 descending track 032 generated using the NSBAS processing chain. Note that the NSBAS-derived result is only shown here for comparison and was not used during the inversion. Green triangles: displacement time-series from ALOS-2 track ascending track A138. Red triangles: displacement time-series from ALOS-2 descending track 027. The light blue and light orange lines correspond to the negative displacement trend for the Sentinel-1 derived measurements. LOS, line-of-sight.

Fig 2

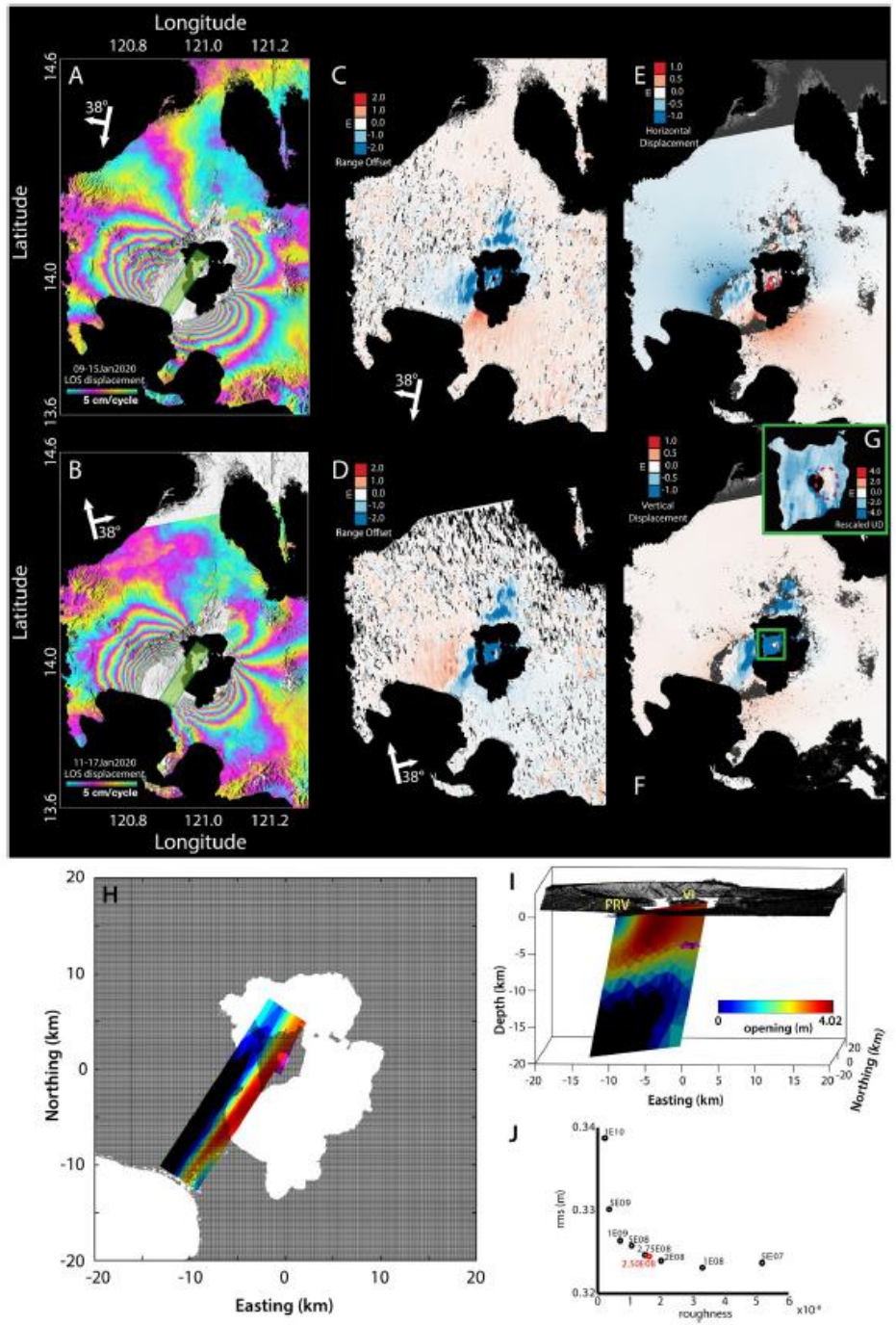

Fig 3

The co-eruptive datasets and model. (a and b) The InSAR phase, re-wrapped at 5 cm per color cycle, and (c and d) range-offset displacement maps from Sentinel-1 descending and ascending tracks showing how much the ground moved as a result of the Taal eruption and dike emplacement. The green rectangles in Figures 3a and 3b is the trace of the dike from the model inversion. (e and f) Derived horizontal and vertical displacements from InSAR phase and range-offset maps. Note that areas covered by fringe aliasing in the InSAR maps are masked and are replaced by range-offset data. (g) Magnified view of the vertical displacement map to highlight the local subsidence within the island and the location of emplaced volcanic deposits (encircled in red). (h) Map view and (i) 3D view of the CDM and distributed opening model. PRV: Pansipit River Valley; VI: Volcano Island. (j) Solution root-mean-square misfit versus roughness as a function of the smoothing value used for the dike. The value in red text is the smoothing factor that we used for the co-eruptive model.

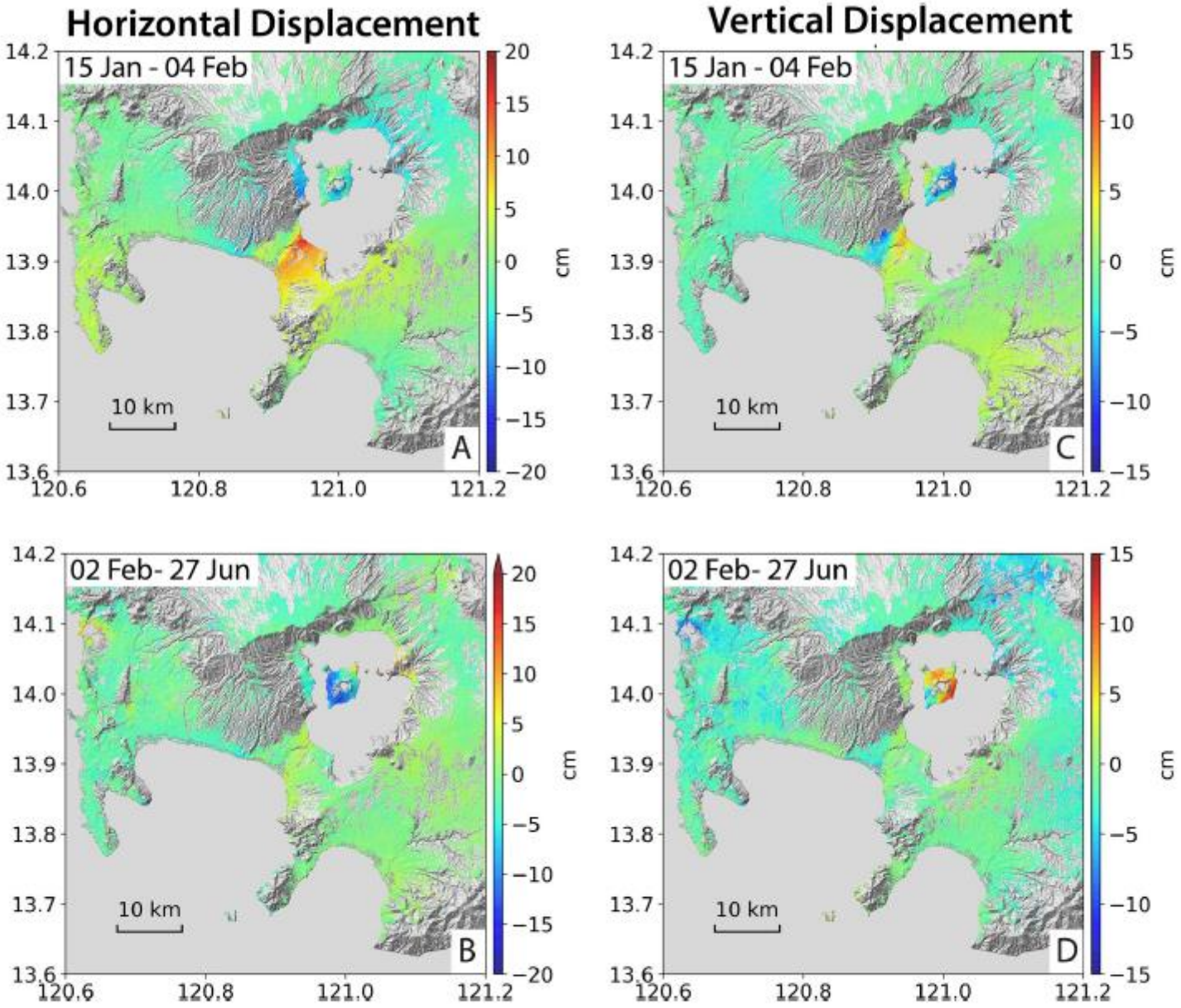

Figure 4. Post-eruptive data. Horizontal (a and b) and vertical displacement (c and d) maps derived using Sentinel-1 descending and ascending datasets covering two periods: (a and c) 15 January to 04 February and (b and d) 02 February to 27 June 2020. (a and b) Red means that the ground moved eastward, blue signifies that the ground moved westward. (c and d) Red means that the ground moved upward and blue represents downward movement.

Fig 4

Geophysical Research Letters

Supporting Information for

The 2020 eruption and the large lateral dike emplacement at Taal volcano, Philippines: Insights from radar satellite data

M. G. Bato[1], P. Lundgren[1], V. Pinel[2], R. Solidum[3], A. Daag[3], M. Cahulogan[3]

[1] Jet Propulsion Laboratory, California Institute of Technology, California, USA

[2] Univ. Grenoble Alpes, Univ. Savoie Mont Blanc, CNRS, IRD, IFSTTAR, ISTerre, Grenoble, France

[3] Philippine Institute of Volcanology and Seismology (PHIVOLCS), Department of Science and Technology (DOST), Quezon City, Philippines

Contents of this file

Introduction

This supplementary file contains text, figures and a table in support of the main document.
Text S1: Text describing a detailed version of our method section in the main text.
Figures S1-S2: Supporting figures for the pre-eruptive modeling.
Figure S3: Pre- to post-January 2020 eruption volume estimates.
Figure S4-S7: Supporting figures for the co-eruptive modeling.
Figures S8-S12: Supporting figures for the post-main eruptive phase time-series analyses.
Figures S13-S17: Supporting figures for the post-main eruptive phase modeling.
Table S1: Prior conditions used for the inversions as well as the derived MAP solutions from the posterior PDFs.

Text S1. Detailed data processing and modeling

Pre-eruptive dataset. For the ALOS-2 SAR data, Earth curvature and topographic effects were corrected based on precise orbits and the SRTM 30-m digital elevation model (DEM). For the Sentinel 1A/B SAR data ARIA uses SRTM 90 m DEM for topographic corrections and relies on precise-orbit ephimerides for orbital correction. All the interferograms were unwrapped using the statistical-cost network-flow algorithm, SNAPHU (Chen & Zebker, 2002) software implemented in ISCE and ARIA. A total of 567 descending and 1004 ascending interferograms were produced by ARIA covering Taal from late 2014 up to January 2020 (i.e. S1 A142: 27 October 2014-11 January 2020, S1 D032: 19 October 2014 – 09 January 2020). For ALOS-2, we produced 12 interferograms for the descending track from 02 December 2018 to 12 January 2020 and nine interferograms for the ascending track from 18 September 2018 to 10 December 2019.

For the Sentinel-1 datasets, we removed interferograms that have an average coherence < 0.6 within the Volcano Island (VI). We also masked pixels that have coherence values that are lower than 0.3-0.35 for both tracks. We applied tropospheric delay corrections using ERA-5 weather models (Jolivet & Agram, 2012) and DEM error corrections (Fattahi & Amelung, 2013) for Sentinel-1, which are all implemented in the MintPy software (Yunjun et al., 2019). For the ALOS-2 data, we did not apply any corrections and masking. The effect of weather models in the pre-eruptive dataset have very minimal impact on the time-series as the amplitude of the surface displacement is larger than the weather-model (and DEM-error) corrections (see Figure S19). However, the corrections were important during the near-real time assessment and monitoring of the volcanic state after the main-eruptive phase.

The NSBAS (Doin et al., 2011) interferograms were 1) produced using the Repeat Orbit Interferometry Package (ROI_PAC) (Rosen et al., 2004) modified to allow TOPSAR data ingestion (Grandin, 2015), 2) unwrapped using the ROI_PAC branch-cut unwrapping algorithm, and 3) corrected for tropospheric delays based on ERA-5 weather models.

Co-eruptive datasets. To produce the InSAR phase maps, SAR data from the descending and ascending orbits were processed using ISCE. During the peak of the crisis, the orbital errors were removed using the restituted orbits provided by the Sentinel-1 Quality Control Subsytem to immediately produce the displacement maps and deliver them at minimal latency, ~3 hours, to PHIVOLCS. However, for this manuscript, we reprocessed all the co-eruptive interferograms and use the precise orbits to correct for orbital errors. We unwrapped the phase using SNAPHU and masked the regions where fringe aliasing are observed. Fringe aliasing arises because of the dense number of fringes that often result from large ground displacements.

To generate the pixel offsets map, we applied pixel offset tracking analysis to the Sentinel-1 SAR images on both tracks implemented within ISCE. The pixel offset analysis cross-correlates the co-registered SAR amplitude images to measure the distortion along the radar line-of-sight (slant range) and along-track (azimuth) directions (Fielding et al., 2020). Because of the lower sampling resolution in the azimuth direction (14 m) compared to the slant range (2.3 m) and the near-parallel orientation of the dike to the azimuth direction,

we only used the range offsets for our analysis. Pixel offset maps complement the InSAR results particularly in regions where fringe aliasing is observed.

Post-eruptive datasets. We followed similar processing steps as those of the co-eruptive method using ISCE to produce the interferograms except that we did not apply a mask. We generated 87 and 69 interferograms from the descending and ascending tracks, respectively.

Pre-eruptive modeling. We used the Caltech-JPL-developed AlTar v2.0 Bayesian inversion software. AlTar is based on the Cascading Adaptive Transitional Metropolis in Parallel method that combines the Metropolis algorithm with elements of simulated annealing and genetic algorithms, allowing the parallel sampling of high-dimensional problems (Minson et al., 2013). We ran 1000 chains x 1000 steps (10^6 samples) starting from uniform distributions (Table S1). Each of the parameter estimates take the form of *a posteriori* probability density functions (PDFs) accounting for the data likelihood and inaccuracies in the data and our prior knowledge about the parameters.

Co-eruptive modeling. For the (1) deflating reservoir and a dike with a uniform opening: we performed Bayesian inversion using the Markov chain Monte Carlo (MCMC) method following Fukuda and Johnson (2010) to find the optimal set of parameters that fit our data (i.e. 10 parameters for the CDM, 8 for the rectangular dislocation, 2 for the InSAR shifts). We started from uniform distributions for each of the model parameters (Table S1) and kept 8 x 10^5 models from the inversion (i.e. we ran 10^6 iterations and burned the first 200,000 models). We derived the optimal values by calculating the MAP solutions. For the (2) deflating reservoir and a dike with distributed opening: we solved for a distributed dike model using a non-negative least squares method (Lundgren et al., 2013). We extended the fault width to 20 km and then discretised this into smaller triangular dislocations before applying a Laplacian smoothing operator to regularize the inversion. We tried several smoothing factors to find the balance between the spatial roughness of the tensile opening and the reduction in the root mean square error.

Pre-eruptive Source Modeling

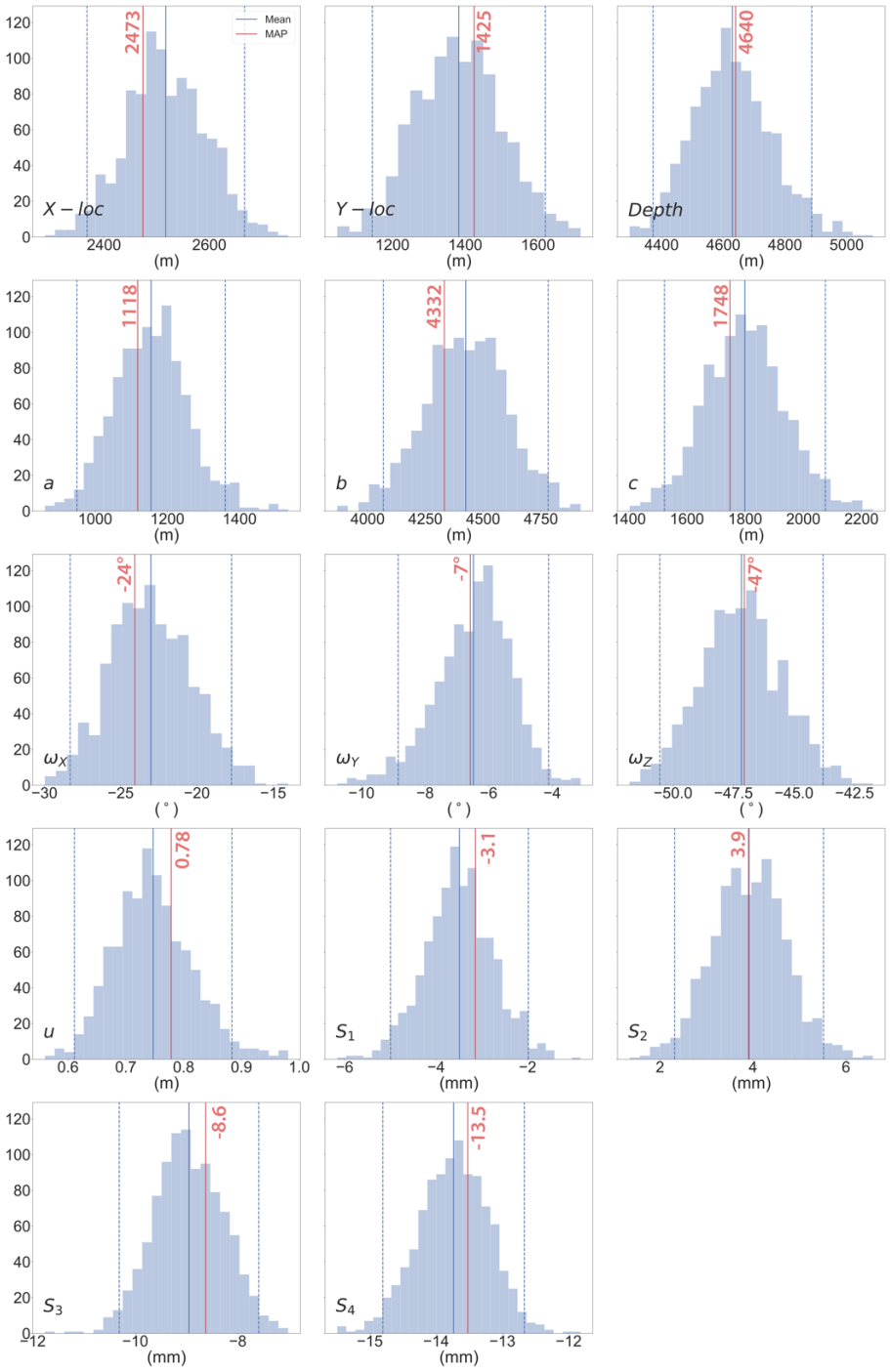

Figure S1. Histograms of each model parameter after the pre-eruptive source modeling using CDM. X- and Y-loc are the x and y locations of the source in meters relative to 14°N and 121°E. The semi-axes lengths are given by [*a, b, c*], the rotations are the [ω_X, ω_Y, ω_Z], the InSAR offsets for each dataset are [S_1, S_2, S_3, S_4] and the opening is *u*. The values in red are the maximum *a posteriori* values (MAP) of each model parameters.

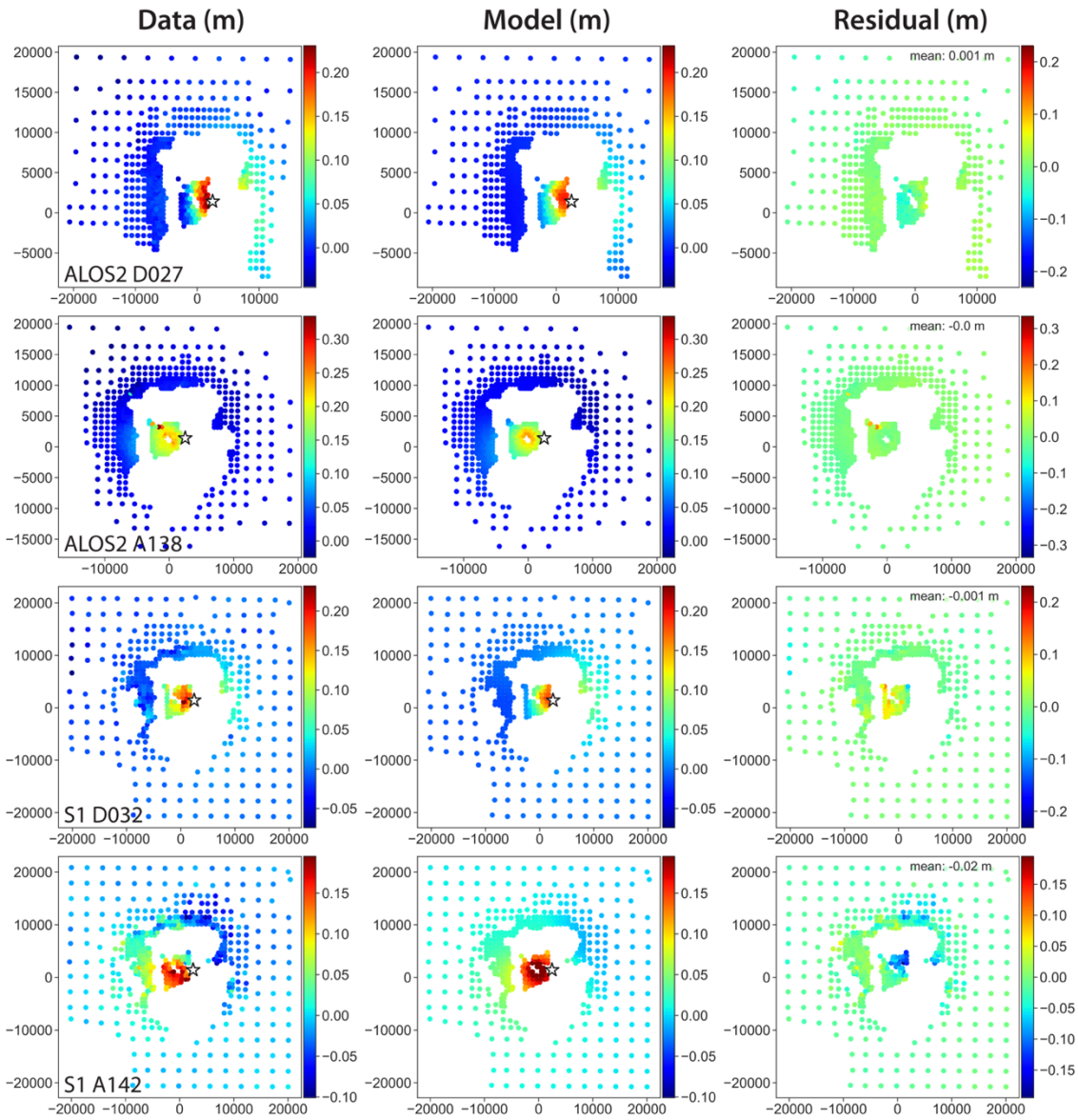

Figure S2. Pre-eruptive source inversion results. Data (left), model (center), and residual (right) for the quadtreed ALOS-2 descending track 027, ALOS-2 ascending track 138, Sentinel-1 descending track 032, Sentinel-1 ascending track 142 displacements, arranged from top to bottom. The white star is the location of the pre-eruptive magmatic source. The axes are in meters relative to 14°N and 121°E.

Volume Estimates

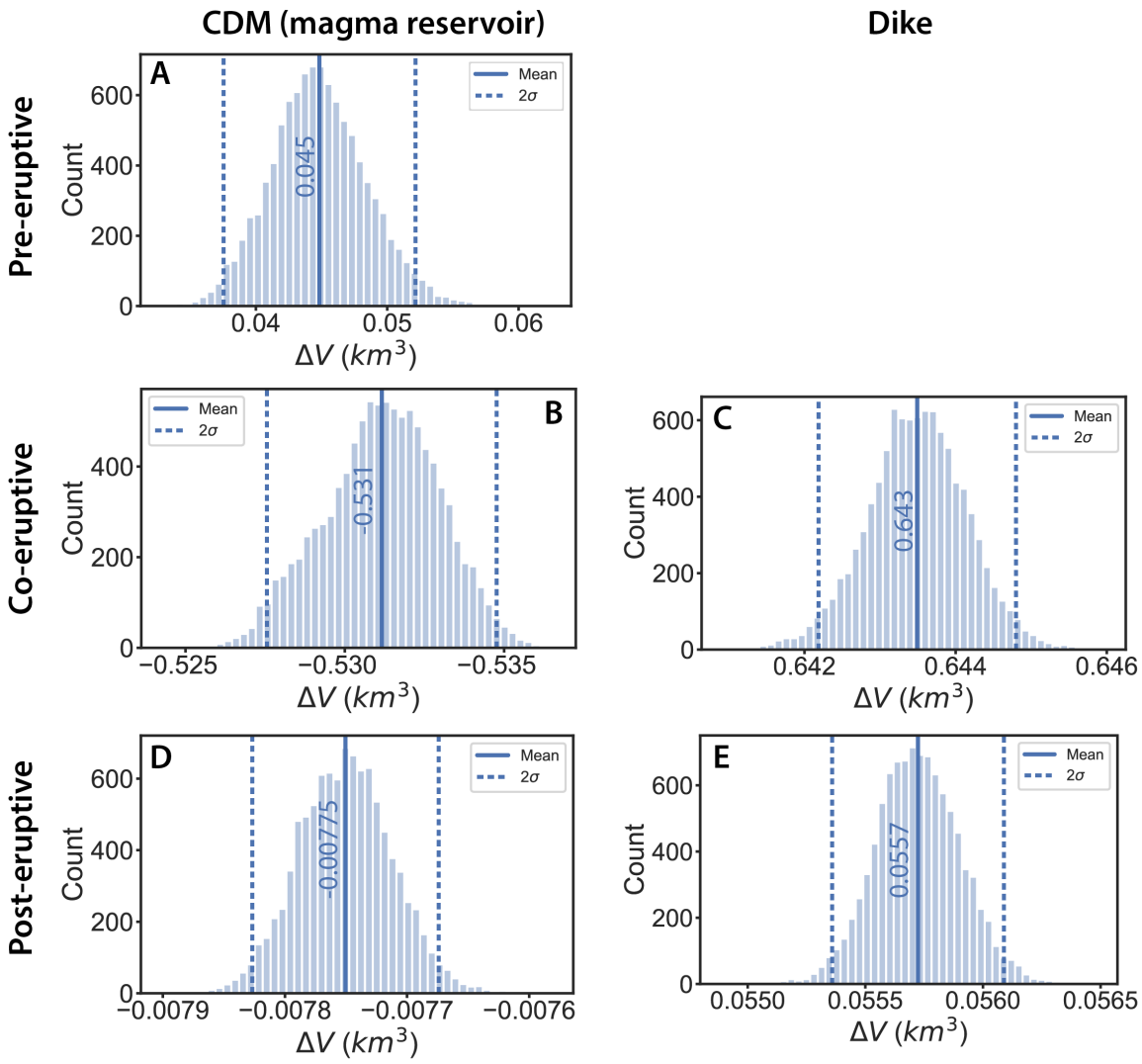

Figure S3. The estimated pre- to post-eruptive volume changes of the CDM (left) and the dike (right) derived from the posterior PDFs of the model parameters. The volume of the CDM (magma reservoir) is calculated using: $\Delta V = 4\ u\ (a\ b + b\ c + a\ c)$. Whereas for the dike volume, we use: $\Delta V = l\ w\ u_3$. We sampled 10000 models from each parameter's posterior distributions to obtain a PDF of the volume change and quantify their respective uncertainties. For the post-eruptive case, we sampled the volume based on the Case-2 modeling approach (i.e. the CDM geometries and locations are fixed given the co-eruptive MAP results) using only the last 50000 MCMC models.

Co-eruptive source modeling

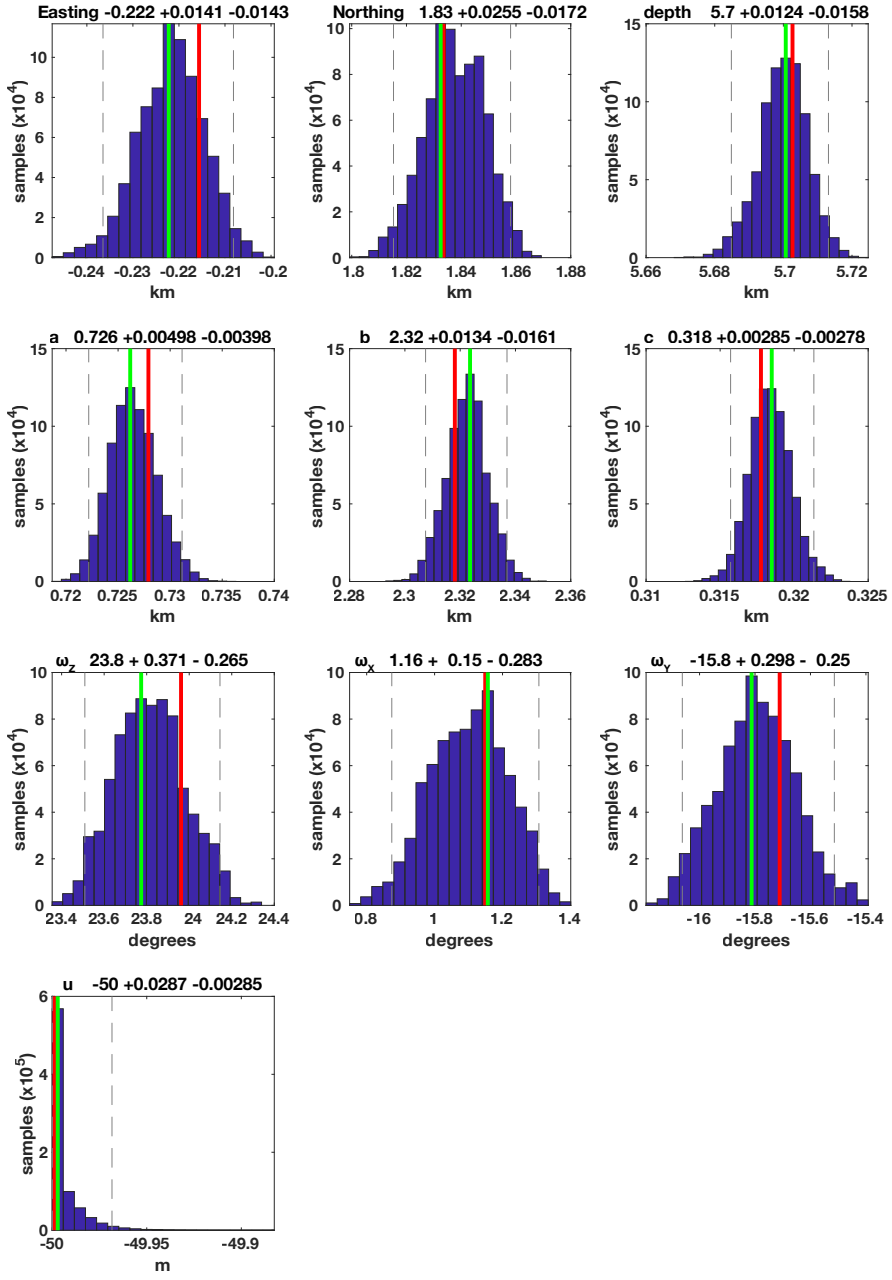

Figure S4. Histograms of each CDM model parameter after the co-eruptive source modeling (i.e. deflating magma reservoir and a dike intrusion). The red lines mark the MAP values of each model parameters whereas the green lines are the mean values. The easting and northing values are given in kilometers relative to 14°N and 121°E. Notice that the negative opening, *u*, falls at the lower bound of our prior. This results from the strong trade-offs between the negative opening and the geometry of the CDM (i.e. semi-axes lengths and the rotations) due to the lack of data constraints within the Volcano Island and in the lake. Hence, in the text, we only reported the volume change of the reservoir.

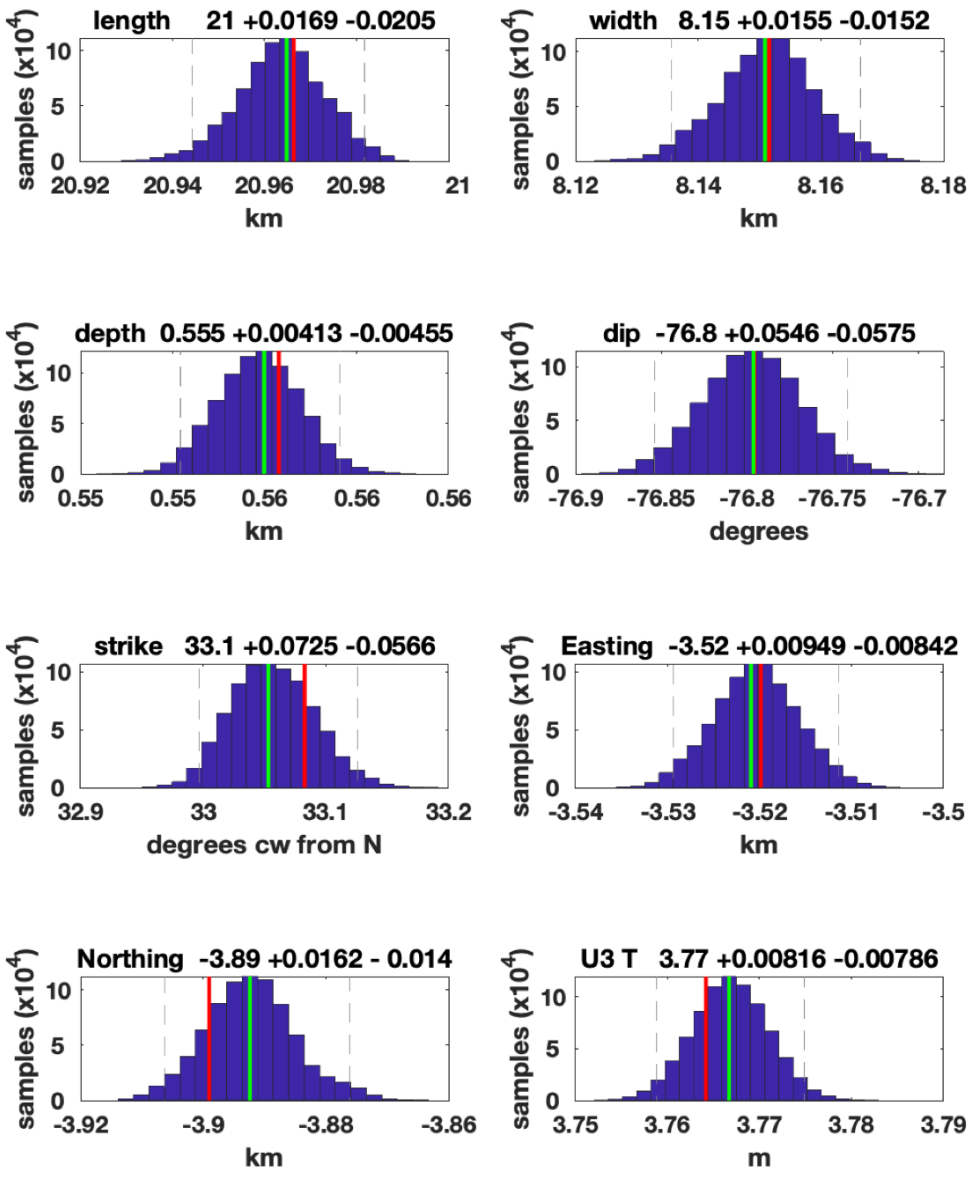

Figure S5. Histograms of each dike model parameter after the co-eruptive source modeling (i.e. deflating magma reservoir and a dike intrusion). The red lines mark the MAP values of each model parameters whereas the green lines are the mean values. The easting and northing values are given in kilometers relative to 14°N and 121°E.

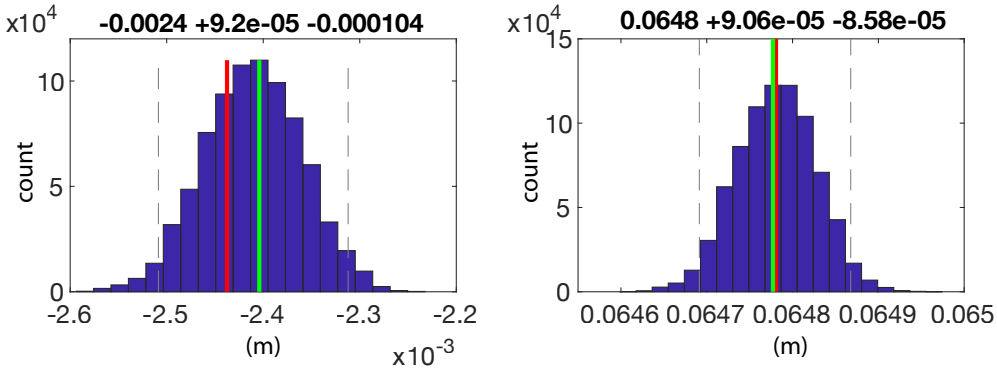

Figure S6. Histograms of the shifts in the InSAR measurements. (Left) Descending track 032 co-eruptive data. (Right) Ascending track 142 co-eruptive data. The red lines mark the MAP values of each model parameters whereas the green lines are the mean values.

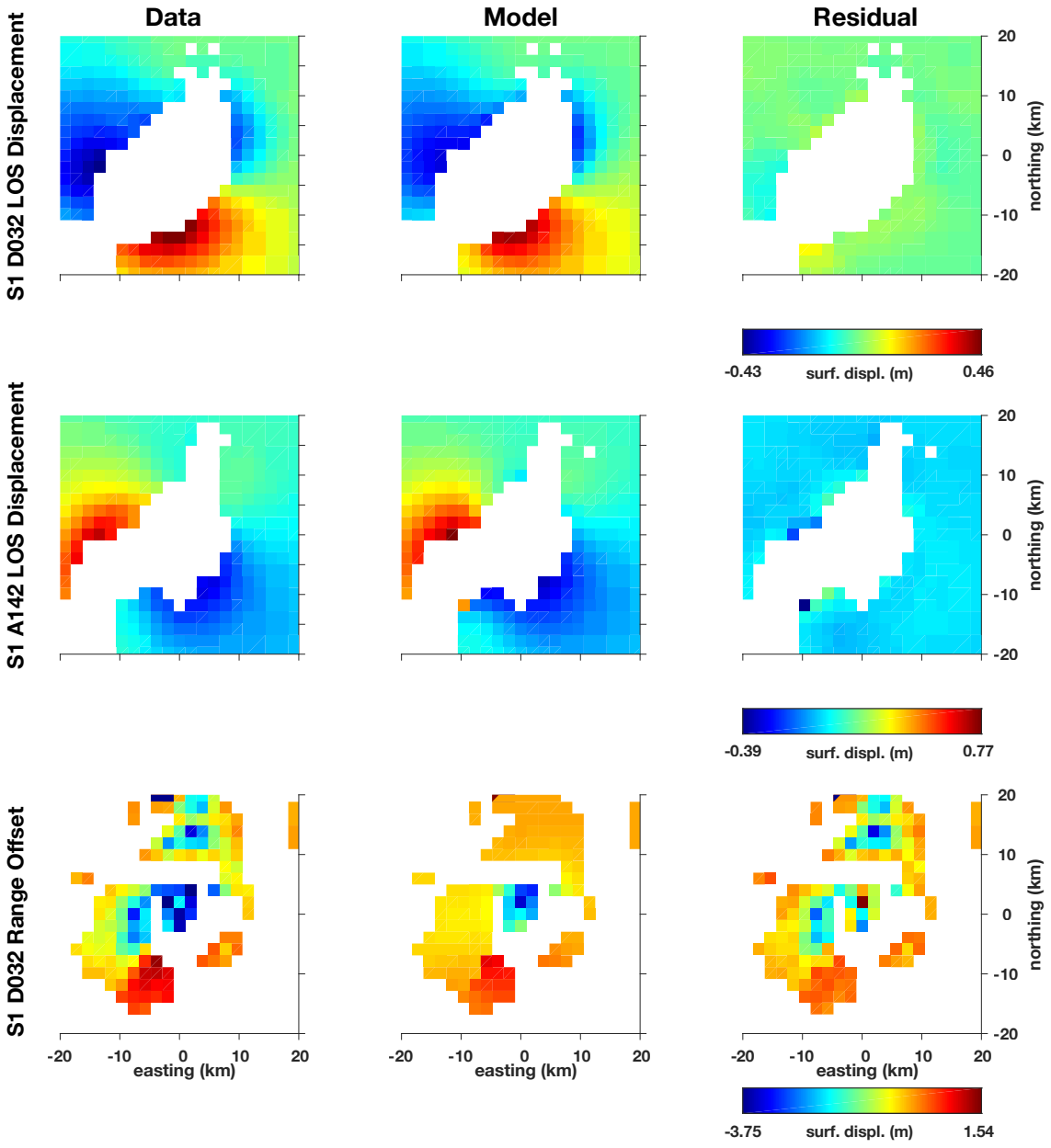

Figure S7. Co-eruptive source inversion results. Data (left), model (center), and residual (right) for the quadtreed Sentinel-1 descending track 032, Sentinel-1 ascending track 142 InSAR-derived displacements, and Sentinel-1 descending track 032 range-offset, arranged from top to bottom. The axes are in kilometers relative to 14°N and 121°E.

Post-eruptive deformation time-series

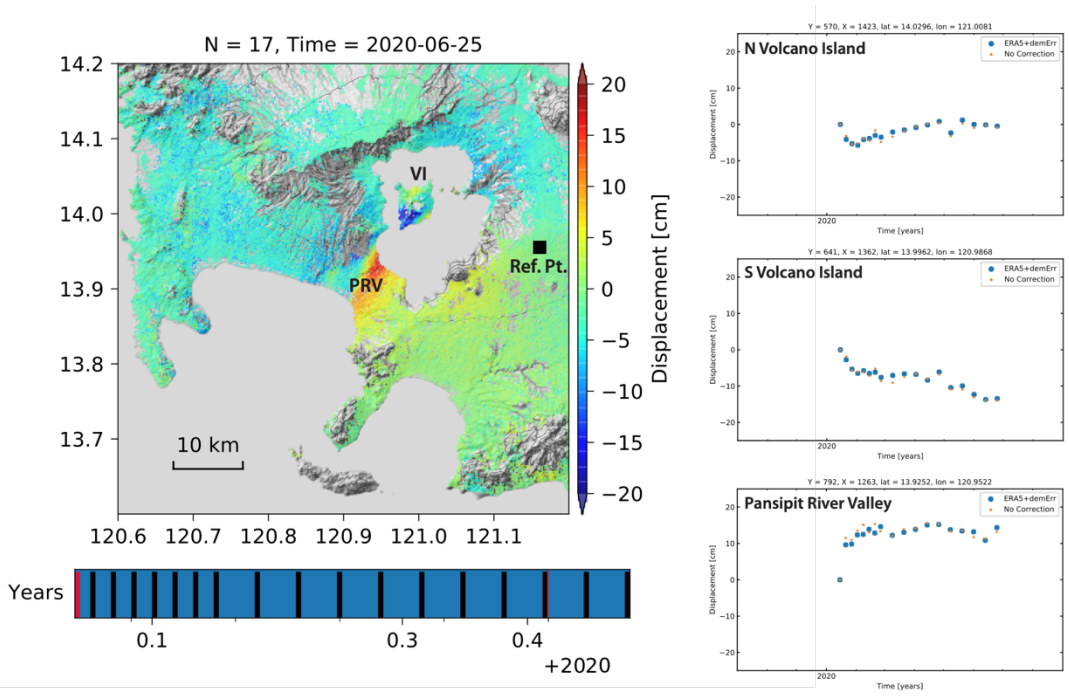

Figure S8. Post-main eruptive phase deformation from descending Sentinel-1 time-series between 15 January and 25 June 2020. (Left) Cumulative deformation map in LOS. Red means that the ground moved toward the satellite, blue corresponds to movement away from the satellite. VI: Volcano Island, PRV: Pansipit River Valley, Ref. Pt.: Reference point. (Right) Deformation time-series at selected points within Taal. Orange dots correspond to the raw time-series, blue dots were corrected for atmospheric noise using ERA-5 weather models, and DEM errors.

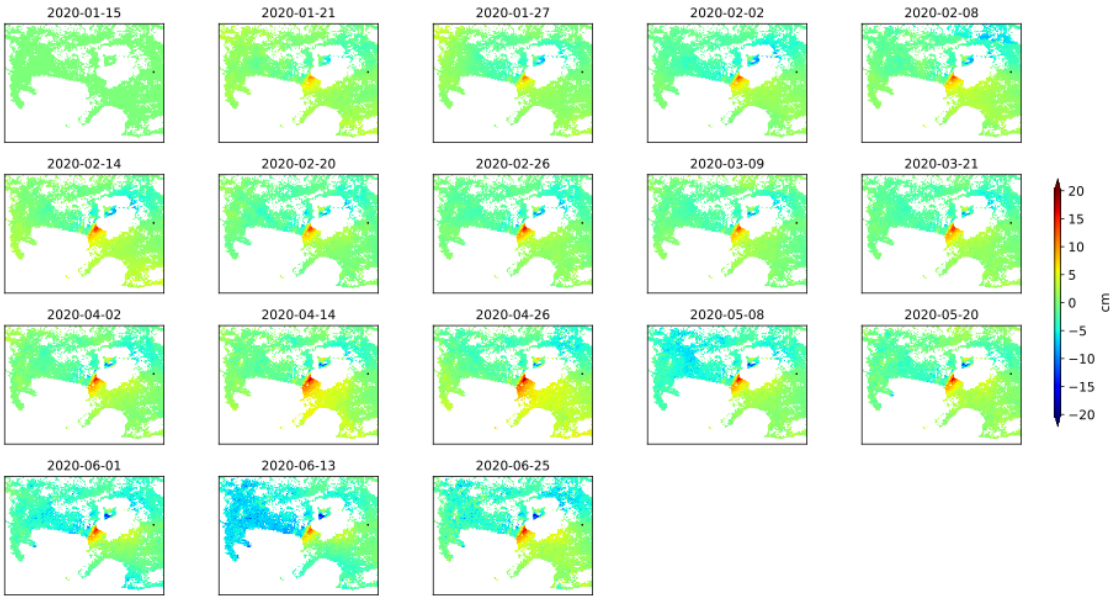

Figure S9. The deformation time-series from the Sentinel-1 descending track after applying atmospheric and DEM error corrections, showing the spatial and temporal evolution of the ground between 15 January and 25 June 2020. Black dot is the reference point. All maps are referenced to the first date (15 January).

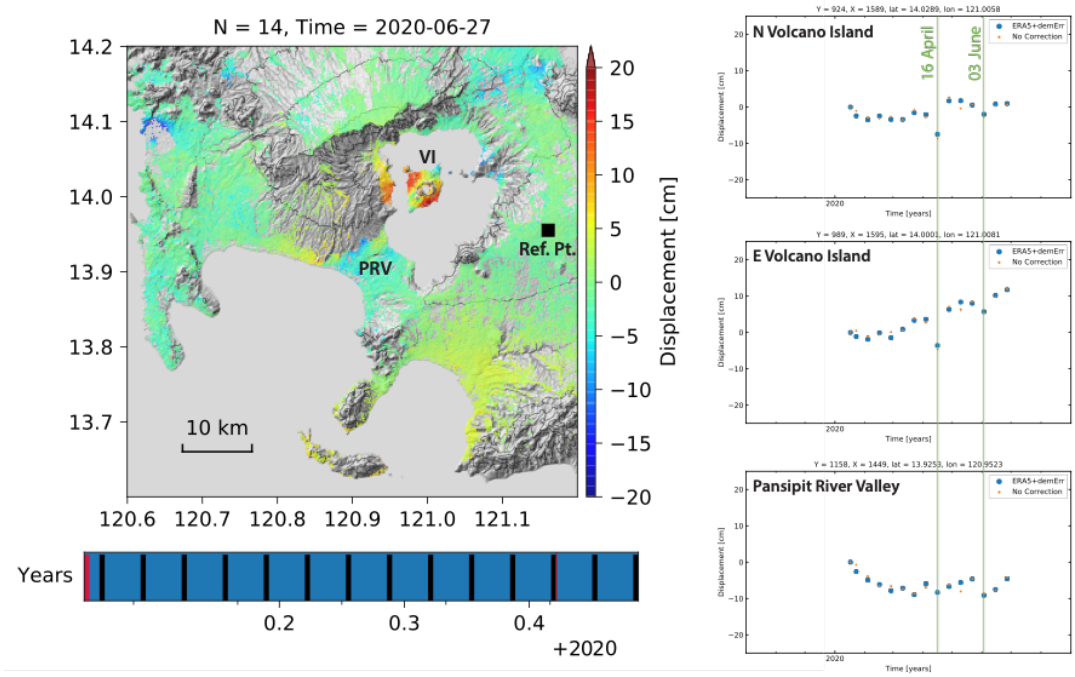

Figure S10. Post-main eruptive deformation from ascending Sentinel-1 time-series between 17 January and 27 June 2020. (Left) Cumulative deformation map in LOS. Red means that the ground moved toward the satellite, blue corresponds to movement away from the satellite. VI: Volcano Island, PRV: Pansipit River Valley, Ref. Pt.: Reference point. (Right) Deformation time-series at selected points within Taal. Orange dots correspond to the raw time-series, blue dots were corrected for atmospheric noise using ERA-5 weather models, and DEM errors.

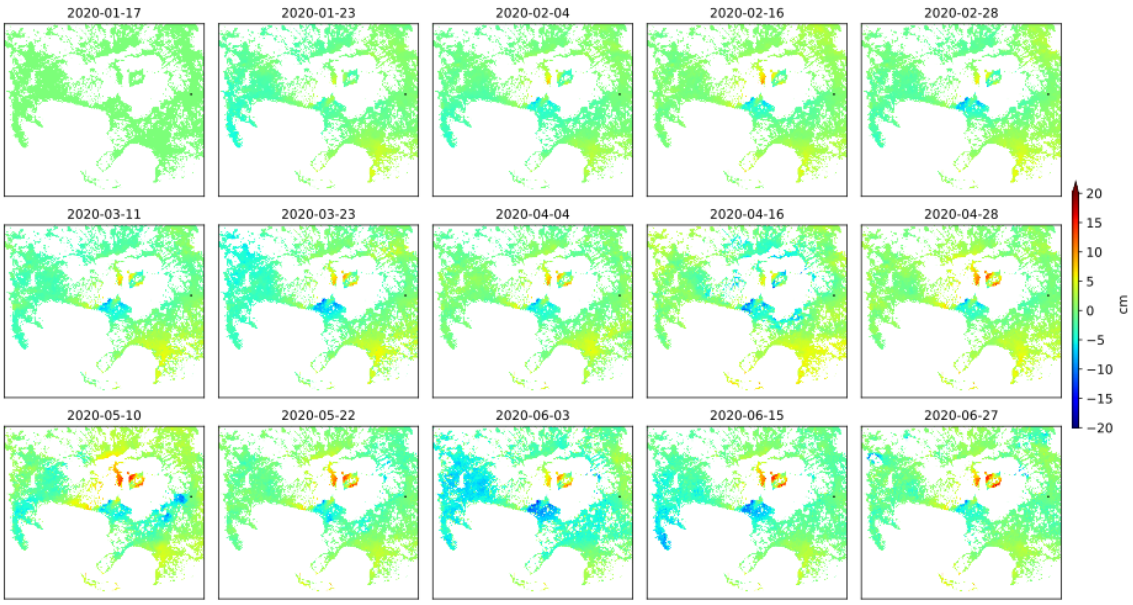

Figure S11. The deformation time-series from the Sentinel-1 ascending track after applying atmospheric and DEM error corrections, showing the spatial and temporal evolution of the ground between 17 January and 27 June 2020. Black dot is the reference point. All maps are referenced to the first date (17 January).

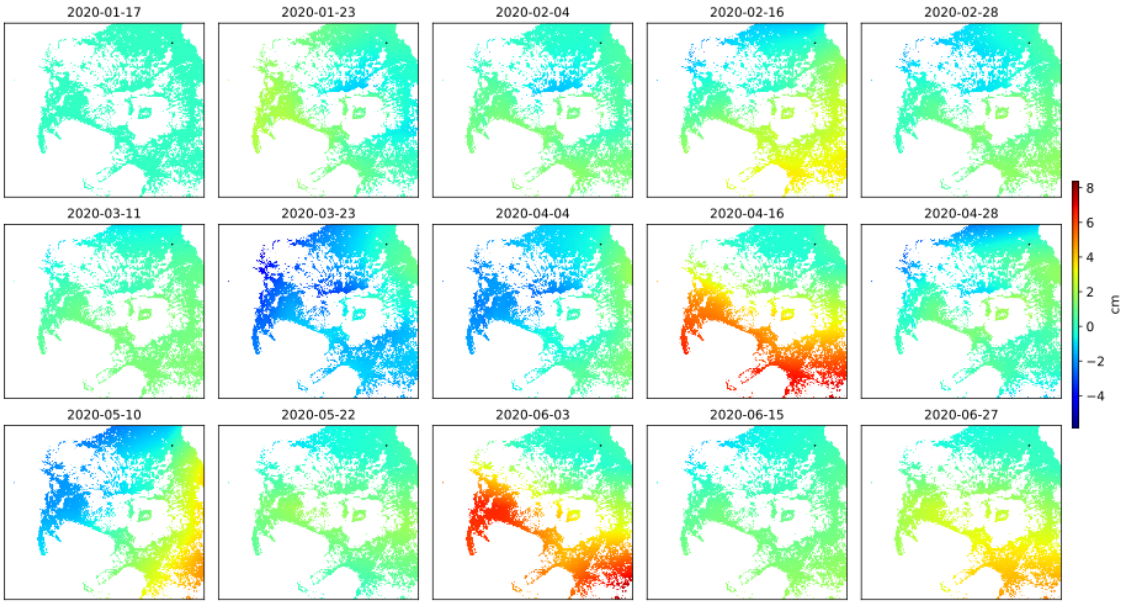

Figure S12. The ERA-5 weather models used in correcting the Sentinel-1 ascending time-series. Notice that on 16 April and 03 June 2020, large atmospheric perturbations (i.e. possibly due to heavy rain/humidity) are observed in this region which may have caused the off-trend points in Figure S10.

Post-eruptive modeling

Case 1: Fixed CDM and dike geometries and locations using co-eruptive MAP solutions

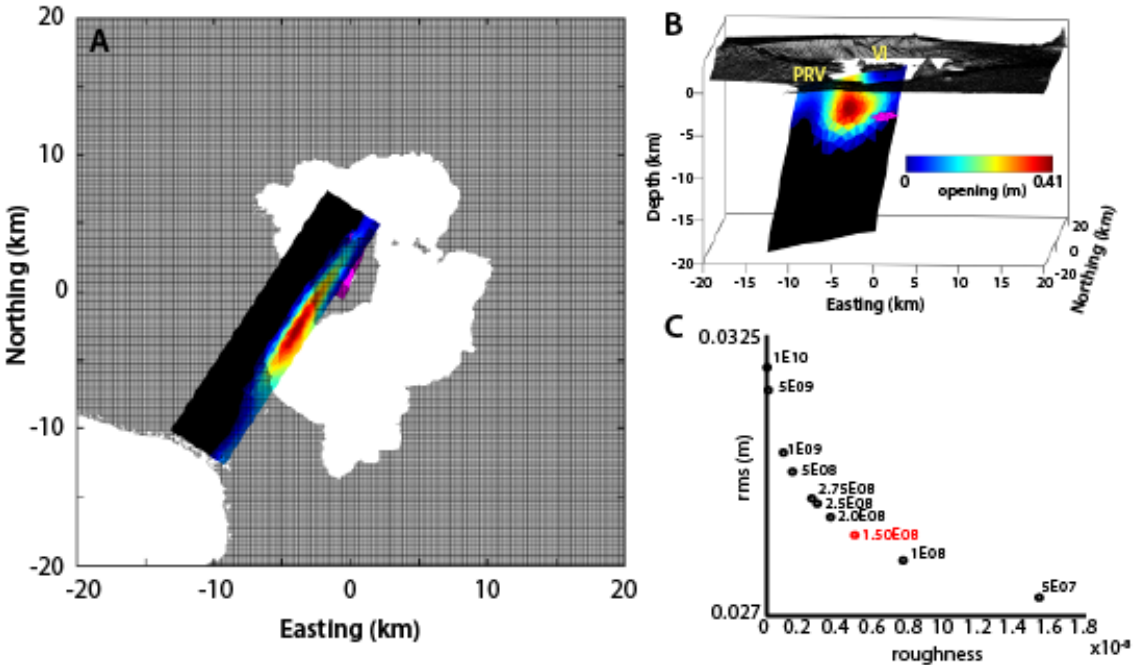

Figure S13. Post-eruptive model for Case 1. (A) Map view and (B) 3D view of the post-eruptive model covering 15 January-04 February 2020. For this model (i.e. post-eruptive model: Case 1), we fixed the geometries and locations of the CDM and the dike using the co-eruptive MAP results (see Table S1). (C) Solution root-mean-square misfit vs. roughness as a function of the smoothing value used for the dike. The value in red text is the smoothing factor that we used for the post-eruptive model.

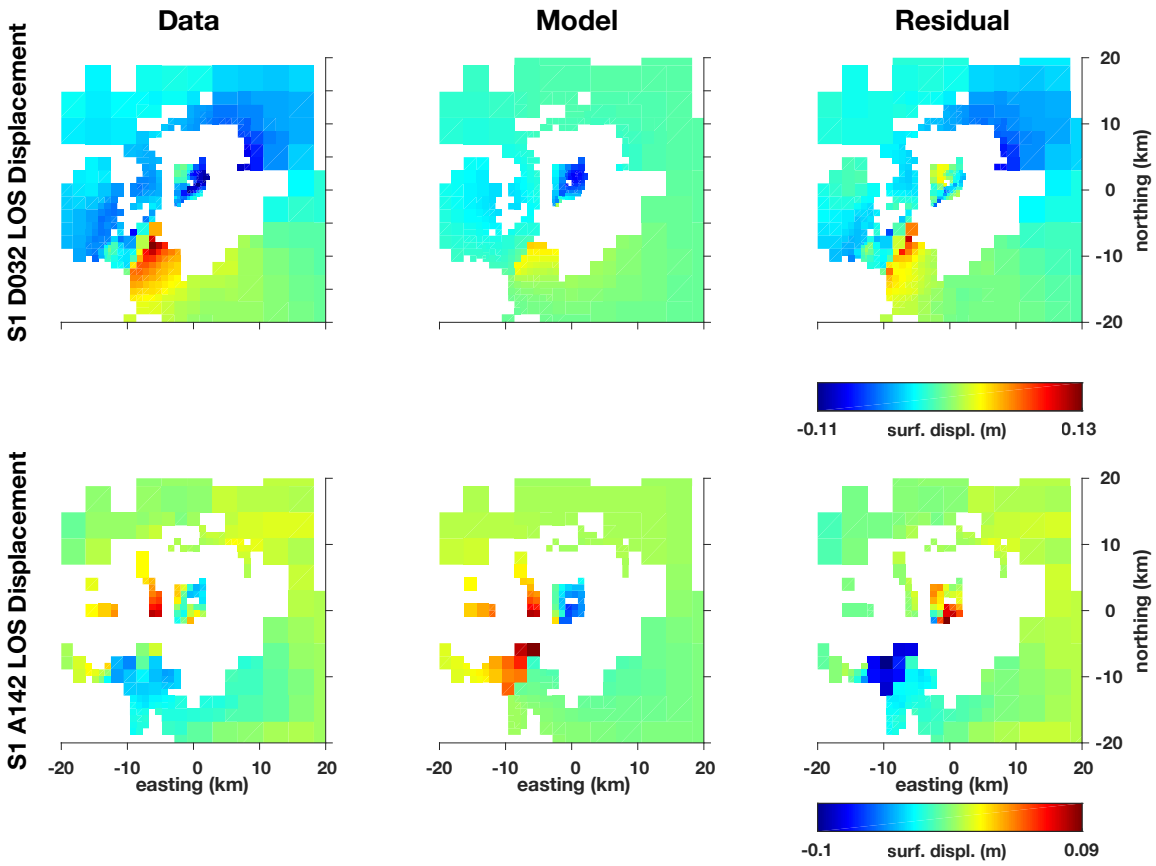

Figure S14. Post-eruptive source inversion results for Case 1 (Figure S13). The geometries and locations of the CDM and the dike were fixed using the co-eruptive MAP values presented in Table S1. Afterwards, we inferred for the negative opening of the CDM and the distributed opening of the dike using non-negative least squares approach. Data (left), model (center), and residual (right) for the quadtreed Sentinel-1 descending track 032, Sentinel-1 ascending track 142 InSAR-derived displacements arranged from top to bottom. The axes are in kilometers relative to 14°N and 121°E.

Case 2: Fixed CDM geometries and locations using co-eruptive MAP solutions. CDM opening and dike parameters are estimated using MCMC

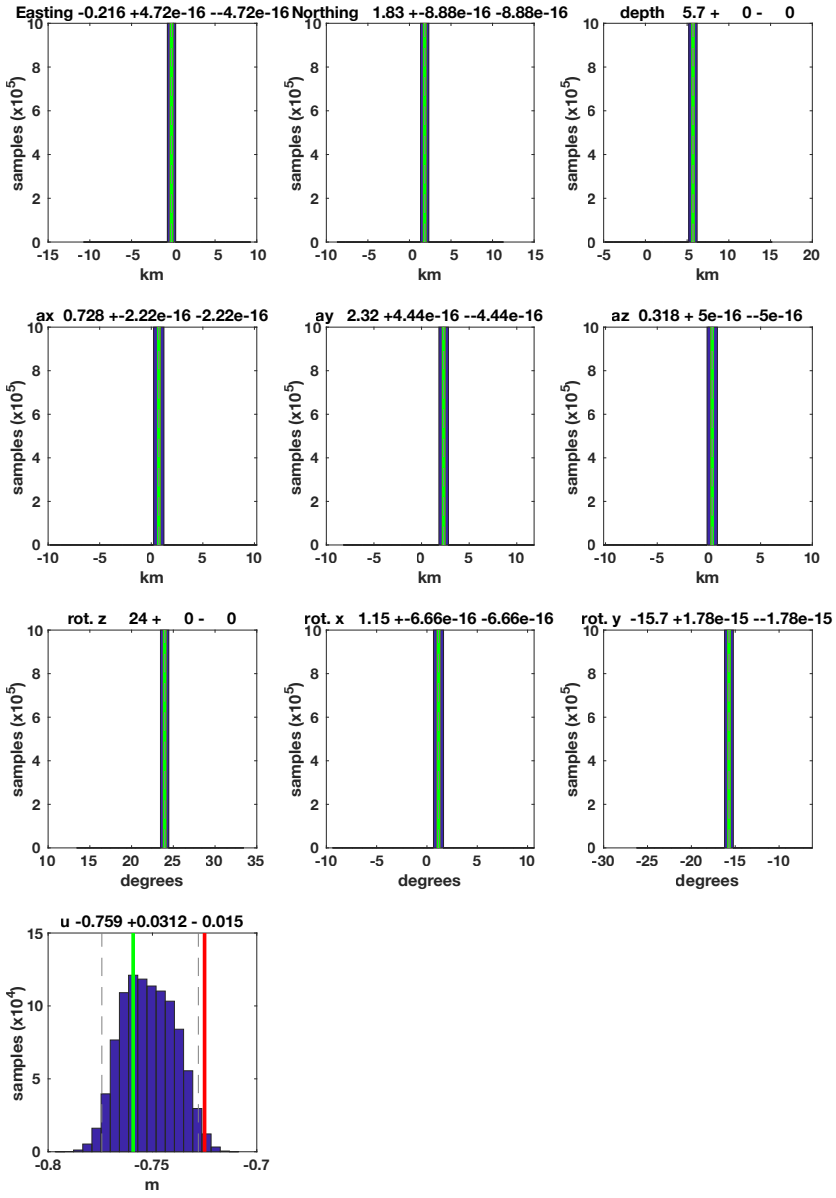

Figure S15. Histograms of each CDM model parameter after the post-main eruptive phase source modeling using MCMC (i.e. deflating magma reservoir and a dike intrusion). Notice that we only inferred for the negative opening of the CDM. The red lines mark the MAP values of each model parameters whereas the green lines are the mean values. The easting and northing values are given in kilometers relative to 14°N and 121°E.

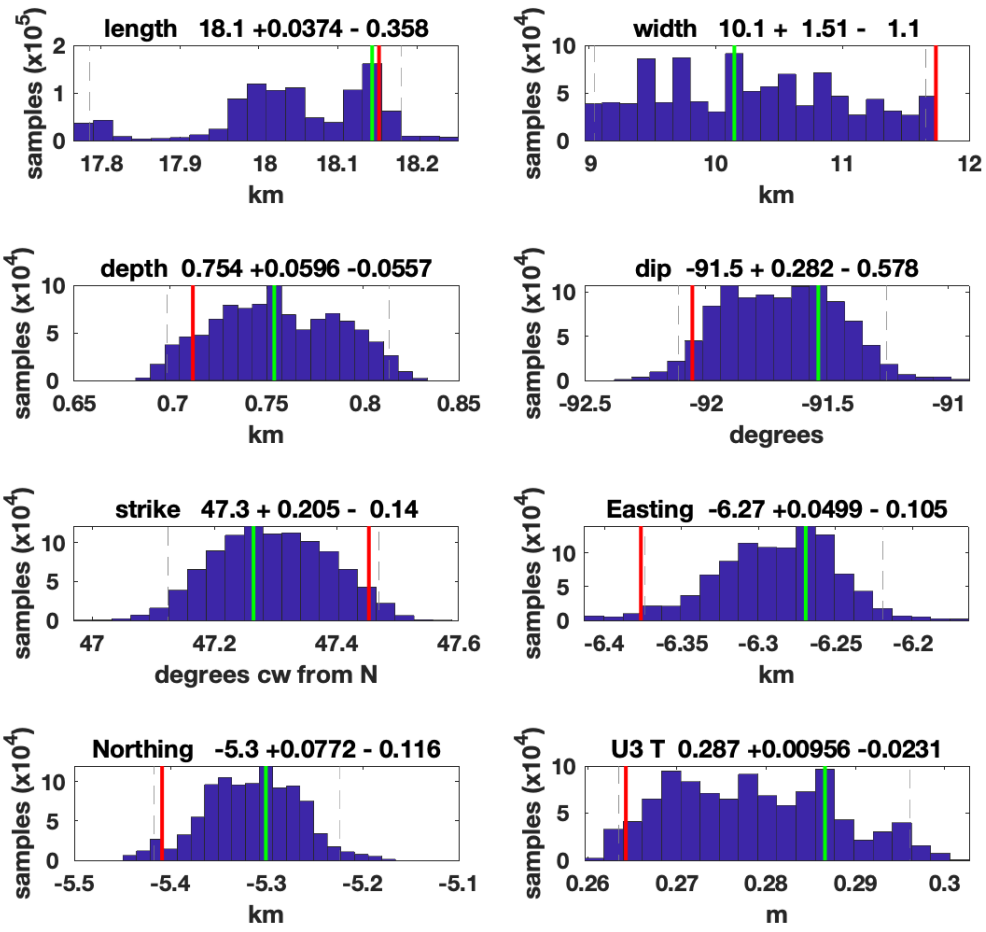

Figure S16. Histograms of each dike model parameter after the post-main eruptive phase source modeling using MCMC (i.e. deflating magma reservoir and a dike intrusion). The red lines mark the MAP values of each model parameters whereas the green lines are the mean values. The easting and northing values are given in kilometers relative to 14°N and 121°E.

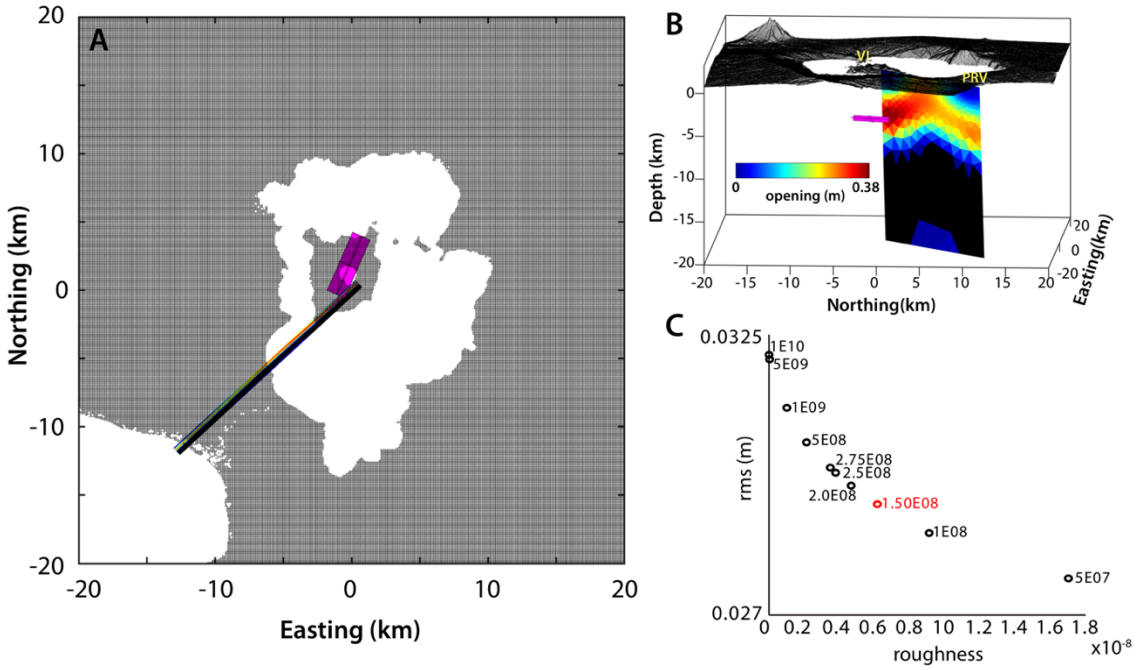

Figure S17. Post-eruptive model for Case 2. (A) Map view and (B) 3D view of the model covering 15 January-04 February 2020. (C) Solution root-mean-square misfit vs. fault slip roughness as a function of the smoothing value used for the dike. The value in red text is the smoothing factor that we used for the post-eruptive model.

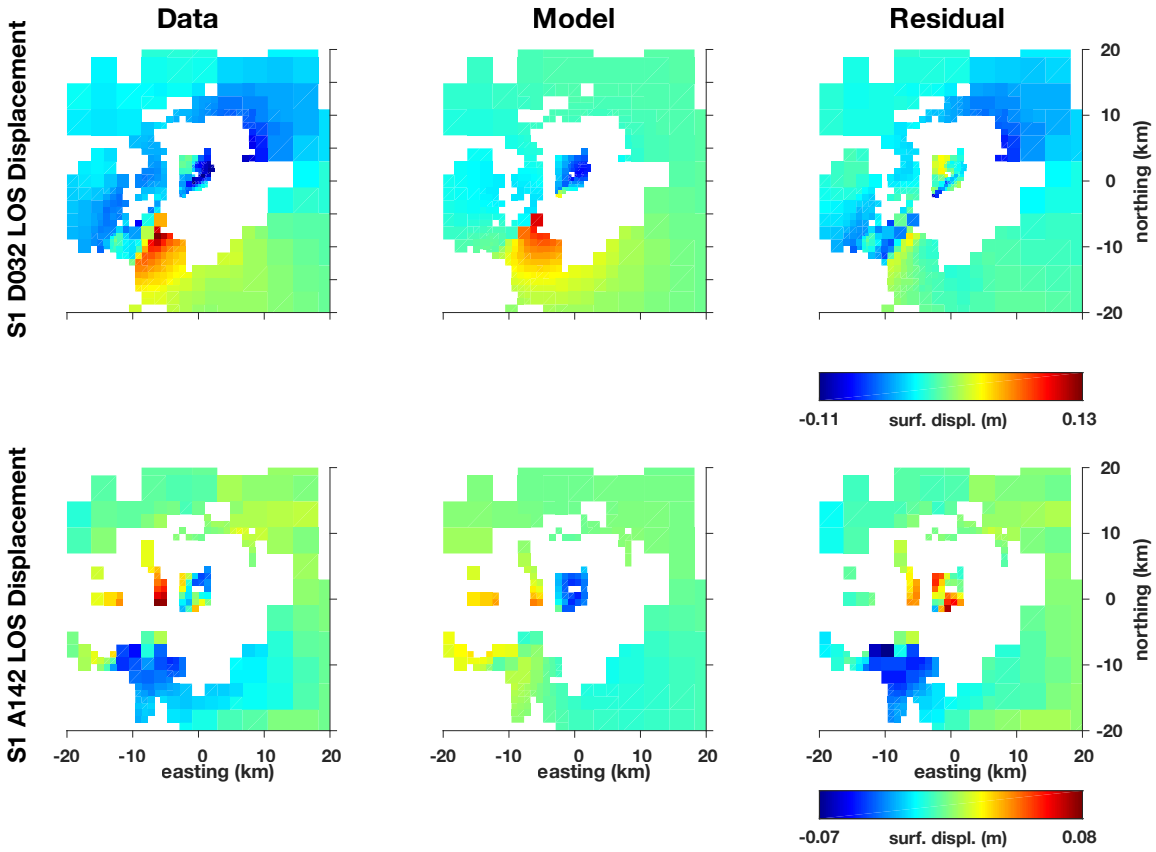

Figure S18. Post-eruptive source inversion result for Case 2. Data (left), model (center), and residual (right) for the quadtreed Sentinel-1 descending track 032, Sentinel-1 ascending track 142 InSAR-derived displacements arranged from top to bottom. The axes are in kilometers relative to 14°N and 121°E.

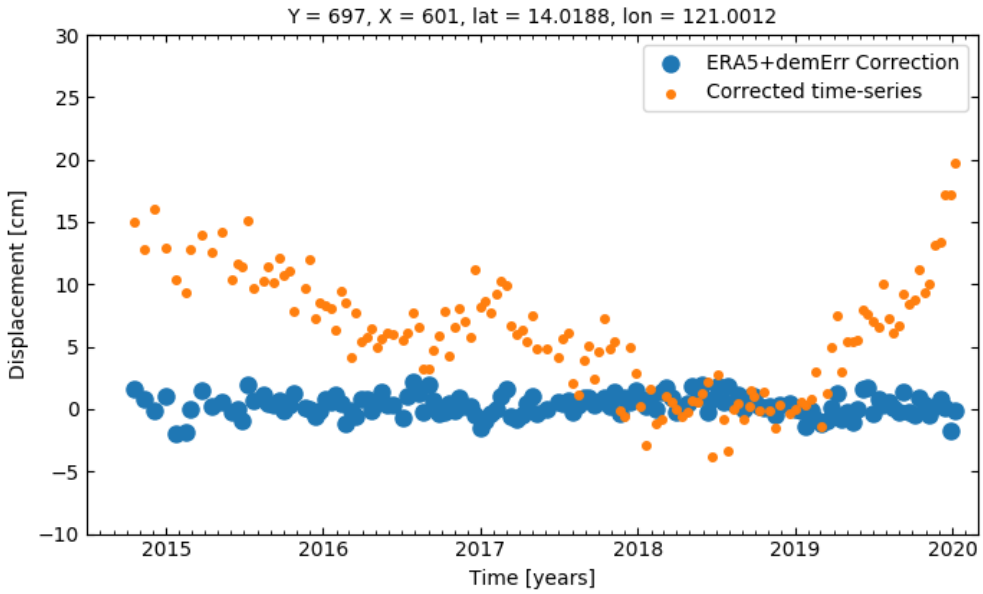

Figure S19. Displacement time-series at 14.0188 °N, 121.0012 °E of ERA5+DEM correction values (blue) and the corrected time-series (orange, as shown in Figure 2C).

Parameter	Pre-eruptive	Co-eruptive		Post-eruptive	
	Prior distribution	Prior distribution	MAP from MCMC	Prior distribution	MAP from MCMC
CDM					
X-location, *X-loc* (km)	U[-10, 10]	U[-5, 5]	0.215	U[-5, 5]	*Coerupt MAP*
Y-location, *Y-loc* (km)	U[-10, 10]	U[-5, 5]	1.833	U[-5, 5]	*Coerupt MAP*
Depth (km)	U[1, 10]	U[0.1, 20]	5.703	U[0.1, 20]	*Coerupt MAP*
Semi-axes lengths:					
a (km)	U[1, 10]	U[0.1, 10]	0.728	U[0.1, 10]	*Coerupt MAP*
b (km)	U[1, 10]	U[0.1, 10]	2.312	U[0.1, 10]	*Coerupt MAP*
c (km)	U[1, 10]	U[0.1, 10]	0.318	U[0.1, 10]	*Coerupt MAP*
Rotations:					
X-rotation, ω_X (°)	U[-30, 30]	U[-89, 89]	1.15	U[-89, 89]	*Coerupt MAP*
Y-rotation, ω_Y (°)	U[-89, 0]	U[-89, 89]	-15.71	U[-89, 89]	*Coerupt MAP*
Z-rotation, ω_Z (°)	U[-89, 0]	U[-180, 180]	23.96	U[-180, 180]	*Coerupt MAP*
Opening, *u (m)*	U[0, 10]	U[-50, 0]	-50	U[-50, 0]	-0.725
Dike					
Length, *l* (km)	--	U[0.1, 40]	20.966	U[0.1, 40]	18.152
Width, *w* (km)	--	U[0.1, 20]	8.152	U[0.1, 20]	11.738
Depth (km)	--	U[0, 15]	0.556	U[0, 15]	0.712
Dip (°)	--	U[-260, 90]	-76.8	U[-260, 90]	-92.1
Strike (°)	--	U[-90, 90]	33.1	U[-90, 90]	47.5
X-location, *Easting* (km)	--	U[-20, 40]	-3.512	U[-20, 40]	-6.376
Y-location, *Northing* (km)	--	U[-20, 10]	-3.899	U[-20, 10]	-5.409
Slip, u_3 (m)	--	U[-5, 15]	3.2	U[-5, 15]	0.264
InSAR offsets (m)	U[-1, 1]	U[-1, 1]	-0.0024 (des); 0.0648 (asc)	U[-1, 1]	-0.0187 (des); 0.0081 (asc)

Table S1. The prior conditions used during the inversions. In the co- and post-eruptive cases, we first inferred for the geometries and locations of the CDM and the dike using MCMC so that we can fix them before computing for the distributed slip. Here, we present the resulting maximum a posteriori (MAP) values after the MCMC inversions. Note that for the post-eruptive modeling, we either used the co-eruptive MAP values or we performed an independent MCMC inversion for the geometries and locations of the dike.

References:

Chen, C. W., & Zebker, H. A. (2002). Phase unwrapping for large SAR interferograms: Statistical segmentation and generalized network models. IEEE Transactions on Geoscience and Remote Sensing, 40(8), 1709-1719.

Doin, M.-P., Guillaso, S., Jolivet, R., Lasserre, C., Lodge, F., Ducret, G., & Grandin, R. (2011). Presentation of the small baseline NSBAS processing chain on a case example: the Etna deformation monitoring from 2003 to 2010 using Envisat data. In Proceedings of the fringe symposium (pp. 3434-3437).

Fattahi, H., & Amelung, F. (2013). DEM error correction in InSAR time series. IEEE Transactions on Geoscience and Remote Sensing , 51 (7), 4249-4259.

Fielding, E. J., Liu, Z., Stephenson, O. L., Zhong, M., Liang, C., Moore, A., … Simons, M. (2020). Surface Deformation Related to the 2019 M w 7.1 and 6.4 Ridgecrest Earthquakes in California from GPS, SAR Interferometry, and SAR Pixel Offsets. Seismological Research Letters.

Fukuda, J., & Johnson, K. M. (2010). Mixed linear —non-linear inversion of crustal deformation data: Bayesian inference of model, weighting and regularization parameters. Geophysical Journal International, 181 (3), 1441-1458.

Grandin, R. (2015). Interferometric processing of SLC Sentinel-1 TOPS data.

Jolivet, R., & Agram, P. (2012). Python-based atmospheric phase screen mitigation using atmospheric re-analysis, 2012. URL: http://pyaps. googlecode.com

Lundgren, P., Poland, M., Miklius, A., Orr, T., Yun, S.-H., Fielding, E., … others (2013). Evolution of dike opening during the March 2011 Kamoamoa fissure eruption, Kilauea Volcano, Hawaii. Journal of Geophysical Research: Solid Earth, 118 (3), 897-914.

Minson, S., Simons, M., & Beck, J. (2013). Bayesian inversion for finite fault earthquake source models I|Theory and algorithm. Geophysical Journal International, 194 (3), 1701-1726.

Rosen, P. A., Hensley, S., Peltzer, G., & Simons, M. (2004). Updated repeat orbit interferometry package released. Eos, Transactions American Geophysical Union, 85 (5), 47.

Yunjun, Z., Fattahi, H., & Amelung, F. (2019). Small baseline InSAR time series analysis: Unwrapping error correction and noise reduction. Computers & Geosciences, 133, 104331.